

# Automatic Selection of Mask and Arterial Phase Images for Temporally Resolved MR Digital Subtraction Angiography

Junhwan Kim,<sup>1\*</sup> Martin R. Prince,<sup>2</sup> Ramin Zabih,<sup>1,2</sup> Jeff Bezanson,<sup>2</sup> Richard Watts,<sup>2</sup> Hale E. Erel,<sup>2</sup> and Yi Wang<sup>2</sup>

**For time-resolved background-subtracted contrast-enhanced magnetic resonance angiography, the bright and sparse arterial signal allows unique identification of contrast bolus arrival in the arteries. This article presents an automatic filtering algorithm using such arterial characterization for selecting arterial phase images and mask images to generate an optimal summary arteriogram. A paired double-blinded comparison demonstrated that this automatic algorithm is as effective as the manual process. Magn Reson Med 48:1004–1010, 2002. © 2002 Wiley-Liss, Inc.**

**Key words:** contrast-enhanced MRA; time-resolved subtraction MRA; image processing; automatic filtering; arteriogram

Contrast-enhanced magnetic resonance angiography (CEMRA) has become a routine clinical tool for pretreatment mapping of vasculature (1). Among data acquisition techniques for CEMRA, the time-resolved strategy offers a very useful option for many situations because of the elimination of the cumbersome timing of imaging to the contrast bolus arrival (2–13). The time-resolved CEMRA generates time series images in a manner similar to fluoroscopic X-ray angiography, where image postprocessing has been used frequently to improve vasculature display (14,15). For example, from the time-series images all mask images and arterial phase images can be summoned into one image of greater vascular detail with high signal-to-noise ratio (SNR) that is particularly useful for presentation in a surgical operation room where video display may not be available. Linear filtering techniques such as the matched filters can be used to produce a summation image (15,16) and have been attempted in time-resolved or dynamic CEMRA to generate a summary arteriogram (17–21). In practice, the major challenge for summarizing time series images is to identify the contrast bolus arrival and to avoid motion-corrupted mask images and arterial phase images that propagate severe motion artifacts into the final summation image (21). So far, this avoidance of motion-corrupted images and selection of optimal arterial phase and mask images for summation have been performed through a tedious manual procedure (21).

Here we report an algorithm that can fully automate the linear filtering process, i.e., to select the set of arterial phase images and the set of mask images such that the subtracted image from the former to the latter is of the best quality. We describe in detail 1) how to quantify the notion of “image quality,” and 2) how to effectively select the mask and arterial phase images based on the quantified measure of quality.

## POSTPROCESSING TECHNIQUES

### Problem Statement

Our approach is basically an automated version of linear filtering that selects a mask image set and an arterial phase image set to generate a linear filtered image. For a given time series of images ( $I_n$ ,  $n = 1 \sim n_{\max}$ ,  $n_{\max} = 35 - 40$ , the total number of images in the time series), indexed by  $x$  and  $y$ , we want to select the mask image set ( $M$ ) and the arterial phase image set ( $A$ ), such that the subtracted or filtered image ( $S_h$ ) is of “best quality,” where  $S_h$  is given by:

$$S_h(x,y) = \sum_{n \in A} I_n(x,y) / |A| - \sum_{n \in M} I_n(x,y) / |M|, \quad [1]$$

where  $|M|$  and  $|A|$  are the number of mask images and arterial phase images, respectively. Note that all the arithmetic operations hereafter are not in the magnitude or real domain as in X-ray angiography (14) but in the complex domain (2), which does not overlook phase information. The key issues in automatic selection of mask images and arterial phase images are 1) how to quantify “image quality,” and 2) how to efficiently select mask and arterial phase images that maximize “image quality.”

### Quantify Image Quality

For a given gray image of size  $256 \times 256$  with intensity range between 0–1, we want to develop an image quality function  $Q$  such that  $Q(I)$  reflects the quality of the image  $I$ . Two basic criteria of a general image are: 1) foreground should be as bright as possible, 2) background should be as dark as possible.

A straightforward way to incorporate those two criteria is to set  $Q(I)$  as the difference between average intensity of the foreground pixels and that of the background pixels:

$$Q(I) = \frac{\sum_{p \in \text{foreground}(I)} I(p)}{|\text{foreground}(I)|} - \frac{\sum_{p \in \text{background}(I)} I(p)}{|\text{background}(I)|} \quad [2]$$

<sup>1</sup>Department of Computer Science, Cornell University, New York, New York.

<sup>2</sup>Department of Radiology, Cornell University, New York, New York.

Grant sponsor: American Heart Association–Heritage Inc.; Grant number: 9951018T; Grant sponsor: National Institutes of Health; Grant numbers: R01 HL60879; R01 HL62994; R01 HL 64647.

\*Correspondence to: Junhwan Kim, Radiology, MRI Research, 515 East 71st Street, New York, NY 10021. E-mail: jkim@cs.cornell.edu

Received 18 January 2002; revised 11 June 2002; accepted 11 June 2002.

DOI 10.1002/mrm.10358

Published online in Wiley InterScience (www.interscience.wiley.com).

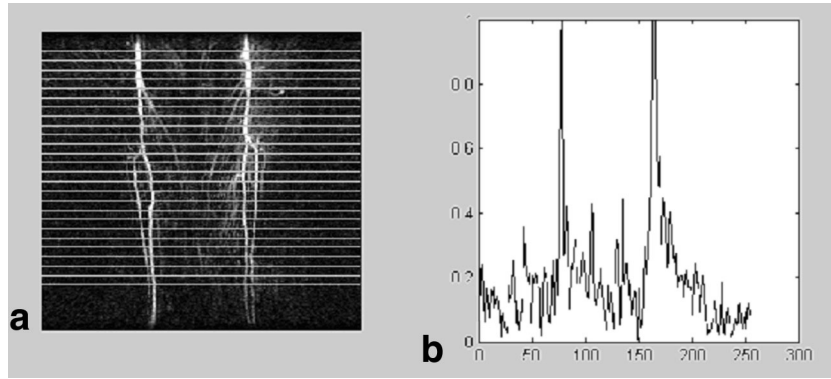


FIG. 1. Image quality evaluation. **a:** Set of scan lines. **b:** Intensity profile of a scan line.

where  $p$  denotes a pixel,  $foreground(I)$  and  $background(I)$  are sets of pixels in  $I$  that belong to the foreground and the background, respectively. Because of interpatient variability, however, it is difficult to determine  $foreground(I)$  and  $background(I)$  a priori. Here we propose to estimate  $foreground(I)$  and  $background(I)$  using image features specific to the application at hand.

Background suppressed or subtracted MRA images have the following features: i)  $foreground(I)$  mainly consists of long vertical lines such as for carotid, aorta, and peripheral arteries (the algorithm applies to horizontal lines for renal arteries with data rotated  $90^\circ$ ); ii) the line width is confined to a specific range, i.e.,  $MinWidth \leq width \leq MaxWidth$ ; iii) for each horizontal scan line, intensity of any foreground pixel is higher than that of any background pixel.

These three features allow a conservative estimation of  $foreground(I)$  and  $background(I)$ . For the  $y$ th horizontal scan line, 1)  $(x, y)$  is in the  $foreground(I)$  if  $I(x, y)$  ranks in brightness between 1st and  $(MinWidth)$ th of 256 pixels in the scan line; 2)  $(x, y)$  is in the  $background(I)$  if  $I(x, y)$  ranks in brightness between  $(MaxWidth + 1)$ th and 256th of 256 pixels in the scan line; 3)  $(x, y)$  is unclassified otherwise. Accordingly,

$$Q(I) \leq \tilde{Q}(I) = \sum_{l=1}^{256} \left( \frac{\sum_{x \in 1st \sim (MinWidth)th} I(x, y)}{MinWidth} - \frac{\sum_{x \in (MaxWidth+1)th \sim 256th} I(x, y)}{256 - MaxWidth} \right). \quad [3]$$

The more accurate the value of  $MinWidth$  and  $MaxWidth$ , the closer  $\tilde{Q}(I)$  approximates  $Q(I)$ . We use  $\tilde{Q}(I)$  as a reasonable estimate for  $Q(I)$ .

The evaluation of  $\tilde{Q}(I)$  in Eq. [3] can be further refined using the following observations: i) For MRA images of the lower extremity, we can split the image vertically into right and left halves and assess the image quality for each half separately, i.e.,  $\tilde{Q}(I) = \tilde{Q}(\text{Left part of } I) + \tilde{Q}(\text{Right part of } I)$ . ii) Because of this similarity between adjacent horizontal scan lines, we can use every fourth or eighth scan line to evaluate image quality, which gives a result very

close to that evaluated at every scan line but increases the computation efficiency by 4- or 8-fold (Fig. 1). iii) A 2–3 cm margin at the highest and lowest edge of the image can be excluded from image quality valuation because of variations due to coil drop-off, gradient warping, field inhomogeneity, and other nonlinear effects. Therefore, the evaluation function for image quality can be implemented as:

$$\tilde{Q}(I) = \sum_{y=1}^{\frac{y_{final}-y_{init}}{y_{step}}+1} \left( \frac{\sum_{x \in 1st \sim (MinWidth)th} I(x, y_{init} + (y-1) \cdot y_{step})}{MinWidth} - \frac{\sum_{x \in (MaxWidth+1)th \sim 256th} I(x, y_{init} + (y-1) \cdot y_{step})}{256 - MaxWidth} \right), \quad [4]$$

where typical values are  $y_{init} = 17$ ,  $y_{final} = 256 - 32$ ,  $y_{step} = 4$  or  $8$ .

### Select Mask and Arterial Phase Images

Once we define the image evaluation function, the next step is to choose the set of mask images ( $M$ ) and the set of arterial phase images ( $A$ ) such that the resulting subtraction image attains maximum quality, i.e., we want to maximize:

$$\tilde{Q}(M, A) \equiv \tilde{Q}(S_h) = \tilde{Q} \left( \sum_{n \in A} I_n / |A| - \sum_{n \in M} I_n / |M| \right) \quad [5]$$

with respect to  $M$  and  $A$ . The selection algorithm consists of the following nine steps:

1. Detect the time point or image frame of contrast arrival ( $n_{ca}$ ).
2. Set the candidate set of mask images,  $M_{All} = 1, 2, 3, \dots, n_{ca} - 1$ .
3. Set the candidate set of arterial phase images,  $A_{All} = n_{ca}, n_{ca} + 1, n_{ca} + 2, \dots, n_{max}$ .
4. Select the pair of the best single mask image  $M_{SingleBest}$  and the best single arterial phase image,  $A_{SingleBest}$ .
5. Initialize the current set of best mask images,  $M_{CurrentBest} = M_{SingleBest}$ .

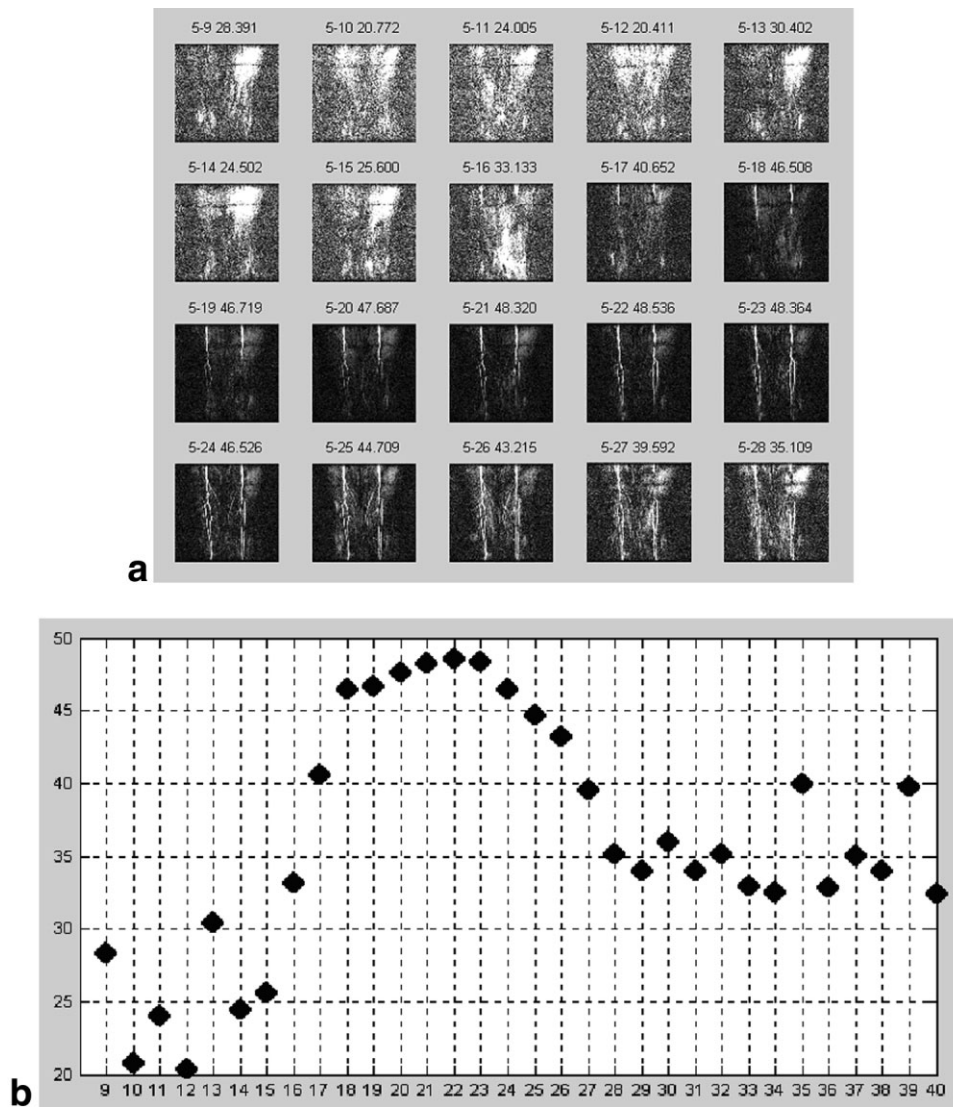


FIG. 2. Contrast arrival detection. **a**: Series of subtraction images between all arterial phase images and one mask image. Note that the window/level is automatically scaled so the brightest pixel has equal intensity in all images. Thus, as contrast arrives (image 17) the increased signal within the artery causes an apparent suppression of background tissues. **b**: Plot of corresponding image quality. Notice that a sharp increase of the image quality function (image 17) corresponds to the contrast arrival in **a**.

6. Initialize the current set of best arterial phase images,  $A_{\text{CurrentBest}} = A_{\text{SingleBest}}$ .
7. Find the set of best arterial phase images that gives the best subtraction image given the current set of best mask images.
8. Find the set of best mask images that gives the best subtraction image given the current set of best arterial phase images.
9. Repeat steps 7 and 8 until convergence.

#### Contrast Arrival Detection (Steps 1–3)

For the contrast arrival detection in Step 1, we only use the top quarter lines in evaluating image quality function  $\tilde{Q}(I)$ . A typical curve of such  $\tilde{Q}(I)$  vs. image index  $n$  is shown in Fig. 2. Contrast usually arrives from the upper part of the image, so we only examine the upper part and

claim that contrast arrives when a sharp increase of  $\tilde{Q}(I)$  is detected.

#### Best Single Pair Selection (Step 4)

Among all possible subtraction pairs of one mask image and one arterial phase image, we select the pair that maximizes the image quality of the filtered image. We currently use  $y_{\text{init}} = 17$ ,  $y_{\text{final}} = 256 - 32$ ,  $y_{\text{step}} = 16$ , for a quick evaluation of image quality.

#### Best Multiple Pair Selection (Steps 5–9)

After initialization of the current set of mask images as the best single mask image at Step 5, the updating of the current set of best arterial phase images in Step 7 consists of the following substeps: 7.i) Sort the arterial phase im-

Table 1  
Summary of Image Quality Comparison Results on the Five Scales and Corresponding Statistical Significances

Image quality distribution	Manual vs. automatic					
	-2	-1	0	1	2	<i>p</i> value (image quality)
Radiologist 1	4	11	2	25	3	0.1533
Radiologist 2	5	17	9	11	3	0.2043
Total	9	28	11	36	6	0.9081

The automatically filtered image is substantially worse [-2], modestly worse [-1], approximately the same [0], modestly better [1], substantially better [2] than the manually filtered image.

ages based on the current set of best mask images. 7.ii) Initialize the current set of arterial phase images as the best single arterial phase image chosen in substep 7.i. 7.iii) Add the next arterial phase image to the current set of best arterial phase images if it improves the image quality of the filtered image. 7.iv) Repeat substep 7.iii for all the arterial phase images. The updating of the current set of best mask images in Step 8 is similar to Step 7.

#### Processing Time

An exhaustive search for the optimal arterial phase images and the optimal mask images requires  $2^{(\# \text{ of all the arterial phase images}) + (\# \text{ of all the mask images})} \sim 2^{30-35} \sim 10^{6-7}$  image quality evaluations. Instead, we use iteration to get a sub-optimal pairs within around 100 image quality evaluations. The overall process takes around 10–12 sec and rarely exceeds 15 sec on a 750 MHz Pentium III PC.

## MATERIALS AND METHODS

### Patients

Forty-five consecutive patients who underwent peripheral MRA including 2D projection MRA of the trifurcation from September 11, 2000, to November 25, 2000, were used for linear filtering using both the manual image selection and the automatic algorithm. These patients included 26 males age 24–87 (mean 70) years and 19 females age 33–85 (mean 68) years. The primary indications for peripheral MRA in these patients included claudication ( $n = 23$ ), limb threatening ischemia ( $n = 11$ ), aneurysm ( $n = 7$ ), post-bypass graft ( $n = 3$ ), and dissection ( $n = 1$ ). This study was approved by our Institutional Review Board.

### Imaging

All data were obtained at 1.5 T using the head coil for signal transmission and reception (LX Horizon, General Electric Medical Systems, Milwaukee, WI). The patients were placed feet-first into the magnet with the legs positioned within the head coil to image from above the patella down to mid-calf. A sagittal gradient echo scout sequence was used to position the coronal 2D projection MRA slab so that it encompassed the entire calf. The 2D projection MRA was performed as a coronal spoiled gradient echo sequence using the following parameters: TR/TE/flip angle = 10/2/60 degrees, slab thickness = 7–10 cm, field-of-view = 30 cm, matrix =  $256 \times 192$ , bandwidth = 16 kHz. The imaging time was 1.95 sec per acquisition for a total of 67 sec to repeat the acquisition 35 times.

Gadolinium contrast (5–7 ml at 0.5mol/L) (Magnevist, Berlex Laboratories, Wayne, NJ; Omniscan, Nycomed Amersham, Princeton, NJ) was injected and flushed with 20 ml saline. The injection rate was 2.5 ml/sec by hand with a SmartSet (TopSpins, Ann Arbor, MI) or using an automatic injector (Spectris MR Injector, MedRad, Pittsburgh, PA). The injection was initiated simultaneously with image acquisition. In this way, at least 5–10 pre-contrast mask images were obtained prior to the arrival the arterial phase at the trifurcation.

### Image Evaluation

To assess this automated method, two radiologists (MRP, HE), blinded to the filtering process, accessed the automatically and the manually filtered images (21) side-by-side using five scales: one image is substantially better than [2], modestly better than [1], approximately the same as [0], modestly worse than [-1], substantially worse than [-2] the other. The orders of the image pair were randomized using a computer and two readers evaluated the images independently. In addition to image quality scoring, the reviewers indicated if first- and second-order branches of the geniculate, anterior tibial, posterior tibial, and peroneal arteries were visible.

### Statistical Analysis

The significance of differences in a paired comparison was determined by performing the paired signed-rank Wilcoxon test (22).

## RESULTS

In the image quality comparison (Table 1), both readers rated the automatic filtering and the manual filtering similarly, with no significant statistical difference. Reader 1 gave slightly better credit for automatic image selection than Reader 2, due to stronger preference for bright foreground detail in spite of additional background noise. Differences in vessel visibility between automatically filtered images and manually filtered images were not discernable (Table 2). For 2 of 45 cases, the automatically filtered image displayed substantially more motion artifact than the manually filtered image. Those images had bright pixels in extraneous structures such as bone edges, which fooled the automatic selection algorithm to make these structures as bright as possible.

Figure 3 is an example in which the automatic filtered image gave substantially more details of foreground com-

Table 2  
Arteries Visualized With Manual and Automatic Linear Filtering

		Geniculate	Branch		AT	Branch		PT	Branch		Peroneal	Branch	
			1st	2nd		1st	2nd		1st	2nd		1st	2nd
Reader 1	Manual	44	30	7	43	25	3	44	31	4	45	22	2
	Automatic	44	36	6	43	29	2	43	29	6	43	18	2
Reader 2	Manual	42	27	3	40	32	1	35	26	4	43	26	3
	Automatic	41	32	5	41	33	1	37	30	5	43	26	2

pared to the manually filtered image. Geniculate arteries are well seen in the automatically filtered image, but poorly visible in the manually filtered image.

Figure 4 is an example of the trade-off between foreground details and background suppression. The automatically filtered image demonstrates better details of distal vessels but slightly poorer proximal vessels and more background noise in the left leg as compared to the manually filtered image. This tortuous vessel case is an example that shows that our algorithm still works even when the assumption that the foreground consists mainly of long, well-behaved vessels does not hold.

Figure 5 is an example where the automatically filtered image and the manually filtered image emphasize the arterial details for different regions. The manually filtered image shows better details of the left popliteal artery, while the automatically filtered image demonstrates better distal tibial arteries as well as the right popliteal artery.

Figure 6 is an example in which the automatic filtering algorithm experiences difficulty when there is very little arterial signal but severe motion artifacts. In the absence of arterial signal, the automatic algorithm enhances extraneous bony structures.

## DISCUSSION

Previously, it was demonstrated that linear filtering of dynamic CEMRA images using a manual procedure generates a convenient summary arteriogram of high SNR and greater vascular details (21). The clinical data from

45 consecutive patients in this study demonstrate that the proposed automatic algorithm for selecting optimal mask images and arterial phase images to generate a linear filtered image works as well as the manual procedure. The typical number of the arterial phase images and the mask images found by the automatic selection program is roughly comparable to those found by the manual method. This automatic image filtering technique is simple and can be easily used in routine clinical practice to process dynamic background-subtracted CEMRA data. The current implementation is being used as a precursor of the manual method in our daily use. Only in the rare case that the automatic selection program gives unsatisfactory results do we use the manual method. Even in that case, we start from the selection given by the automatic selection program instead of starting from scratch.

The cornerstone of the automatic filtering algorithm is the image quality characterization based on the fact that arterial signal in dynamic subtraction CEMRA is the brightest and its spatial distribution is sparse (Fig. 1). Accordingly, an image quality function can be designed to locate the arterial signal by grasping the few brightest pixels in a line perpendicular to the artery of interest (Eq. [4]), and the sharpest increase in the image quality corresponds to the contrast bolus arrival in the artery of interest (Fig. 2). Based on maximizing this image quality, an iterative algorithm is used to select mask images and arterial phase images to generate a linearly filtered image of the highest quality (Eq. [2]).

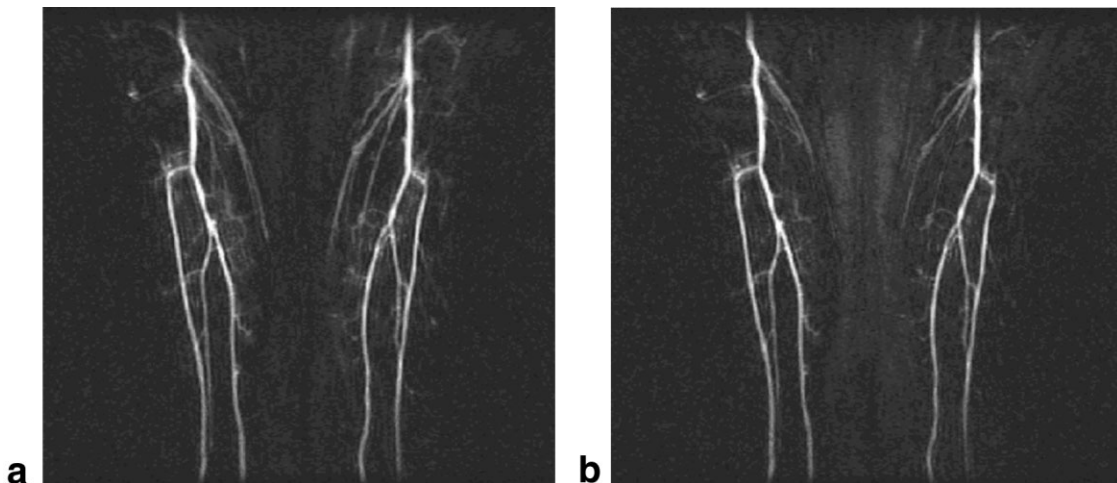


FIG. 3. Coronal 2D MRDSA of Patient 44. **a**: Automatic filtering. **b**: Manual filtering. Image quality comparison = {1 for reader 1 and 2 for reader 2}. Geniculate arteries are better seen in (a) automatically filtered image, compared to (b) manually filtered image.

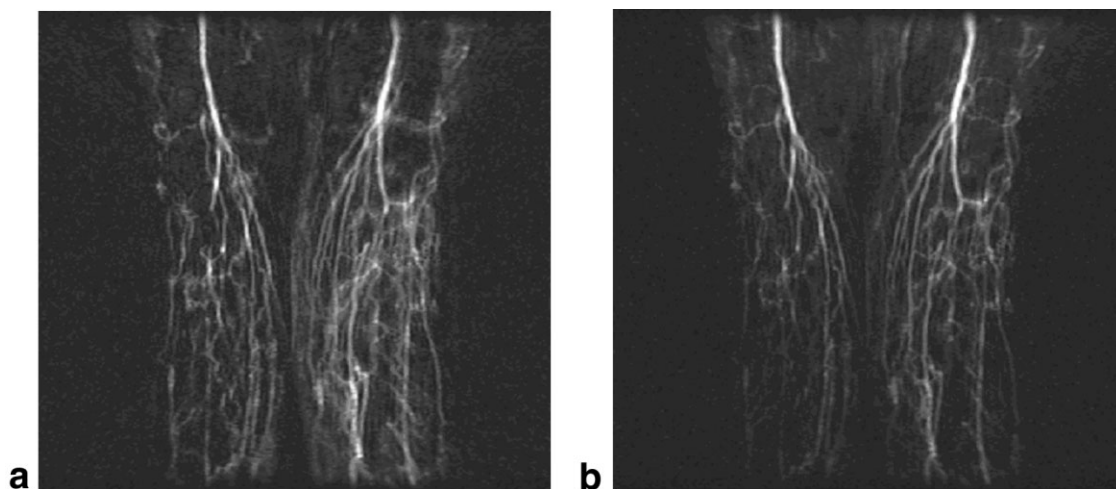


FIG. 4. Coronal 2D MRDSA, Patient 31. **a**: Automatic filtering. **b**: Manual filtering. Image quality comparison =  $\{-1$  for reader 1 and 0 for reader 2}. The automatically filtered image (**a**) shows more details of distal arteries but more background noise in the left leg, whereas the manually filtered image (**b**) depicts slightly better proximal arteries.

The automatic image selection algorithm presented in this article works quite well in suppressing common motion artifacts in dynamic 2D projection MRA that consists of a crowd-like background noise of low signal intensity. Of course, in the absence of bright arterial signal, line-shaped sharp bright artifacts from tissue edges may confuse the current algorithm (Fig. 6), but fortunately this is not the common case. Also, the assumption that the artery width is small is not always correct; for example, for large vessel disease such as aortic aneurysms. Nevertheless, our algorithm gives reasonable results unless other structure is brighter than the artery. In that case, the automatic algorithm enhances extraneous structures.

While it is possible to correct for motion effects by detecting motion displacement and compensating for the phase shifts (23), this automatic linear filtering technique provides significant reduction in motion artifacts by dis-

carding images contaminated with motion. The simple and robust property of this automatic technique validates its routine application in a practical setting.

The current implementation of the automatic selection algorithm (now downloadable from [www.pcmri.com](http://www.pcmri.com)) serves as a preliminarily feasibility test and can be refined in the following way. Current image quality evaluation function in Eq. [4] assesses image quality for both left and right legs together. When motion of the left leg and motion of right leg are different, the optimal selection for the overall image quality may not be optimal for both legs. In the future, separate optimization for each leg would result in better image quality. Images for both legs can be merged seamlessly unless one leg is overlapped with the other.

In summary, an evaluation function was developed to characterize the arterial image quality of time-resolved contrast-enhanced MRA and, based on this function, an

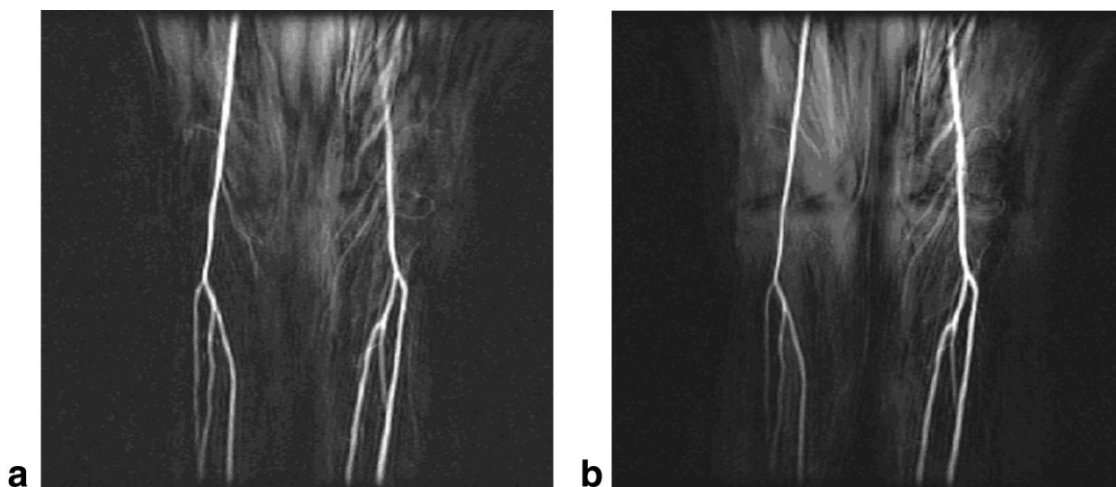


FIG. 5. Coronal 2D MRDSA, Patient 42. **a**: Automatic filtering. **b**: Manual filtering. Image quality comparison =  $\{1$  for reader 1 and 0 for reader 2}. **b**: Manually filtered image shows better detail of the left popliteal artery, while the automatically filtered image (**a**) demonstrates better distal tibial arteries as well as the right popliteal artery.

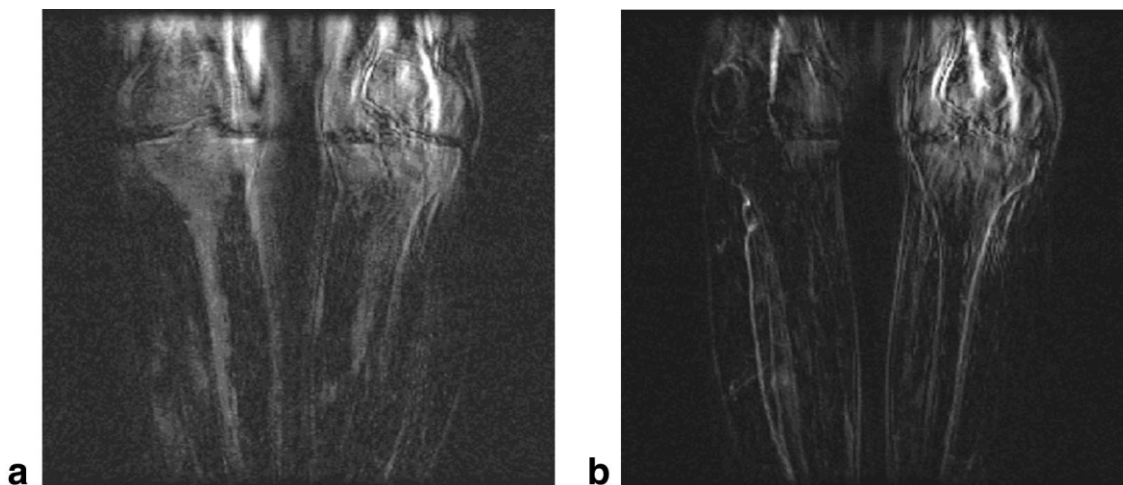


FIG. 6. Coronal 2D MRDSA, Patient 33. **a**: Automatic filtering. **b**: Manual filtering. Image quality comparison = {−2 for both readers}. The automatic filtering algorithm has difficulty when there is very little arterial signal but severe motion artifacts. The automatic filtering algorithm enhanced extraneous bony structures.

algorithm was constructed to automatically select mask images and arterial images for linear filtering that works as effectively as the manual image selection.

## REFERENCES

- Prince MR, Grist TM, Debatin JF. 3D contrast MR angiography, 2nd ed. New York: Springer; 1998.
- Wang Y, Johnston DL, Breen JF, Huston J 3rd, Jack CR, Julsrud PR, Kiely MJ, King BF, Riederer SL, Ehman RL. Dynamic MR digital subtraction angiography using contrast enhancement, fast data acquisition, and complex subtraction. *Magn Reson Med* 1996;36:551–556.
- Korosec FR, Frayne R, Grist TM, Mistretta CA. Time-resolved contrast-enhanced 3D MR angiography. *Magn Reson Med* 1996;36:345–351.
- Hennig J, Scheffler K, Laubenberg J, Strecker R. Time-resolved projection angiography after bolus injection of contrast agent. *Magn Res Med* 1997;37:341–345.
- Mistretta CA, Grist TM, Korosec FR, Frayne R, Peters DC, Mazaheri Y, Carrol TJ. 3D time-resolved contrast-enhanced MR DSA: advantages and tradeoffs. *Magn Reson Med* 1998;40:571–581.
- Winchester PA, Lee HM, Khilnani NM, Wang Y, Trost DW, Bush HL Jr, Sos TA. Comparison of two-dimensional MR digital subtraction angiography of the lower extremity with x-ray angiography. *J Vasc Intervent Radiol* 1998;9:891–900.
- Takano K, Utsunomiya H, Ono H, Okazaki M, Tanaka A. Dynamic contrast-enhanced subtraction MR angiography in intracranial vascular abnormalities. *Eur Radiol* 1999;9:1909–1912.
- Schoenberg SO, Wunsch C, Knopp MV, Essig M, Hawighorst H, Laub G, Prince MR, Allenberg JR, Van Kaick G. Abdominal aortic aneurysm. Detection of multilevel vascular pathology by time-resolved multiphase 3D gadolinium MR angiography: initial report. *Invest Radiol* 1999;34:648–659.
- Klisch J, Strecker R, Hennig J, Schumacher M. Time-resolved projection MRA: clinical application in intracranial vascular malformations. *Neuroradiology* 2000;42:104–107.
- Ludman CN, Yusuf SW, Whitaker SC, Gregson RH, Walker S, Hopkinson BR. Feasibility of using dynamic contrast-enhanced magnetic resonance angiography as the sole imaging modality prior to endovascular repair of abdominal aortic aneurysms. *Eur J Vasc Endovasc Surg* 2000; 19:524–530.
- Turski PA, Korosec FR, Carroll TJ, Willig DS, Grist TM, Mistretta CA. Contrast-enhanced magnetic resonance angiography of the carotid bifurcation using the time-resolved imaging of contrast kinetics (TRICKS) technique. *Top Magn Reson Imag* 2001;12:175–181.
- Wang Y, Winchester PA, Khilnani NM, Lee HM, Watts R, Trost DW, Bush HL, Kent CK, Prince MR. Contrast enhanced peripheral MRA from abdominal aorta to pedal arteries: combined dynamic 2D and bolus chase 3D acquisitions. *Invest Radiol* 2001;36:170–177.
- Goyen M, Ruehm SG, Jagenburg A, Barkhausen J, Kroger K, Debatin JF. Pulmonary arteriovenous malformation: characterization with time-resolved ultrafast 3D MR angiography. *J Magn Reson Imag* 2001;13: 458–460.
- Kruger RA, Riederer SJ. Digital subtraction angiography. Boston: G.K. Hall Medical Publishers; 1984. p 197–219.
- Kruger RA. A method for time domain filtering using computerized fluoroscopy. *Med Phys* 1981;8:466–470.
- Wang Y, Weber DM, Korosec FR, Mistretta CA, Grist TM, Swan JS, Turski PA. Generalized matched filtering for time-resolved MR angiography of pulsatile flow. *Magn Reson Med* 1993;30:600–608.
- Kaandorp DW, Kopinga K, Wijn PF. Venous signal suppression in 3D dynamic Gd-enhanced carotid artery imaging using the eigenimage filter. *Magn Reson Med* 1999;42:307–313.
- Strecker R, Scheffler K, Klisch J, Lehnhardt S, Winterer J, Laubenberg J, Fischer H, Hennig J. Fast functional MRA using time-resolved projection MR angiography with correlation analysis. *Magn Reson Med* 2000;43:303–309.
- Bock M, Schoenberg SO, Floemer F, Schad LR. Separation of arteries and veins in 3D MR angiography using correlation analysis. *Magn Reson Med* 2000;43:481–487.
- Blasbalg R, Mitchell DG, Outwater EK, Ito K, Gabata T, Chiowanich P. Free MRA of the abdomen: postprocessing dynamic gadolinium-enhanced 3D axial MR images. *Abdom Imag* 2000;25:62–66.
- Prince MR, Yoo SK, Watts R, Kim J, Zabih R, Wang Y. Mask averaging to improve 2D projection MRA of peripheral arteries. In: Proceedings of the XIII Annual International Workshop on MRA, Madison, WI, 2001. p 84.
- Zar JH. Biostatistical analysis, 3rd ed. Upper Saddle River, NJ: Prentice Hall; 1996. p 123–178.
- Ehman RL, Felmlee JP. Adaptive technique for high-definition MR imaging of moving structures. *Radiology* 1989;173:255–263.